High Entropy Alloys & Materials
https://doi.org/10.1007/s44210-024-00029-z

ORIGINAL PAPER

Additively Manufactured Lightweight and Hard High-Entropy Alloys by Thermally Activated Solvent Extraction

Prince Sharma[1] · Chayan Das[1] · Praveen Sreeramagiri[1] · Ganesh Balasubramanian[1]

Received: 1 November 2023 / Accepted: 24 January 2024

Abstract
We introduce a scalable thermally activated solvent extraction based additive manufacturing process to produce lightweight, yet high-hardness, multicomponent alloys. The cost-effective process involves layer-wise curing a slurry composed of AlCoCrFeNi high-entropy alloy powder and a transparent ultraviolet-sensitive photopolymer, by stereolithography 3D printing followed by sintering. The alloy pellets assume a density of 4.3 g/cm^3 and hardness of 400 HV with a BCC/FCC multiphase microstructure. A broad distribution in the particle sizes of the alloy powder augments the manufacturing process because the smaller particles operate as fillers to weld the larger ones. The relatively higher surface energy of the smaller particles limits the activation energy required for the onset of particulate diffusion that instigates the necking. Microscopic characterization reveals passivating surface oxides on the powder particles fabricating an alloy part suitable for harsh environments.

Keywords High-entropy alloys · Additive manufacturing · Sintering · Lightweight · Porosity · Hardness

Introduction

The concept of multicomponent *a.k.a.* multi-principal element alloys (MPEAs) as first introduced by Cantor et al. [1], initiates a transformative paradigm of alloying multiple (> 4, quaternary) elements with near equiatomic compositions that crystallize into a stable single-phase random solid-solution. In parallel, Yeh et al. [2] elucidate the metallurgical phenomenon by emphasizing the significant role of the high configurational entropy of mixing, surpassing a threshold of > 1.39R or 11.54 J/mol K for equiatomic quaternary MPEAs [3–5]. This elevated configurational entropy essentially dominates the thermodynamic stability attributed to the enthalpy of formation [5, 6]. These alloys, subsequently termed as high-entropy alloys (HEAs), rapidly gained attention as several of the compositions reproduced exceptional mechanical properties as well as thermal and chemical stabilities under extreme environments [2, 7–12]. While HEAs can encompass millions of new possible compositions, stable solid-solutions have been predominantly limited to alloys comprising of *3d* and *4d* transition elements, which assume high densities and render the alloys heavy. Cellular/hierarchical structural configurations of HEAs can enable their potential for lightweight structural components applicable in aeronautics, hypersonics, transportation, biomedical and chemical industries [7–16].

Additive manufacturing (AM), a.k.a. 3D printing, has revolutionized manufacturing by layered deposition of materials to synthesize specimens guided by computer aided design with unprecedented form flexibility and complexity [17]. AM involves the sequential addition of material to enable the creation of complex and customized structures with increased efficiency relative to traditional (i.e., subtractive) manufacturing methods [17, 18], whence the fabrication of fine cellular structures remains challenging. AM is the emergent technique for the synthesis of intricate microlattices, cellular, hierarchical structures, and honeycomb-like configurations with high geometric complexity [19, 20]. This capability is particularly beneficial for light-weighting structures that employ heavy refractory HEAs, where the optimized cellular configurations can enhance performance efficiency without compromising strength [21–23]. AM allows for greater design flexibility, reduced material waste, and the ability to produce customized, highly complex geometries, making it a preferred method for fabricating advanced structures with HEAs [21–25]. Recent literature demonstrates the

✉ Ganesh Balasubramanian
biganesh@gmail.com

[1] Department of Mechanical Engineering & Mechanics, Lehigh University, 19 Memorial Drive West, Bethlehem, PA 18015, USA

Published online: 15 February 2024

synthesis of cellular HEAs by direct ink writing and binder jetting, that do not require melting and leverage pressure-less sintering to densify the part to a desired level; the inclusion of designer porosity fractions contribute to the reduced densities [26–29]. CoCrFeNi HEA microlattice fabricated by direct ink writing reveals superior performance under cryogenic conditions [30]. The tensile strength of CoCrFeNiMn HEA samples synthesized by injection molding followed by sintering across different temperatures [31], are comparable to alloys produced by casting and spark plasma sintering. 3D printed porous (67%) iron via an extrusion- based method [32] is able to assume an interconnected and biodegradable cellular structure, as are 3D printed Fe–Mg porous scaffolds that are found to be MRI-friendly and biodegradable [33]. Likewise, highly porous 316L stainless steel manufactured via binder jetting [34] assumes elastic properties equivalent to that produced by conventional route. Nonetheless, scalability to industrial specimens with low production cost are challenges that limit the wider implementation of some of the above approaches. Additionally, this method is cost effective considering the machinery and setup cost as compared to most of the other techniques of additively manufactured porous materials namely, selective laser melting [35], laser powder bed fusion [36], wire arc additive manufacturing [37], electron beam manufacturing [38]. To address these shortcomings, we introduce a novel thermal solvent extraction-based AM process leveraging stereolithography (SLA) and sintering to produce lightweight HEAs. As elaborated below from the characterization, the smaller particles serve as fillers to weld larger particles, rendering a hardness of ~ 400 HV and density of ~ 4.3 g/cm^3.

Experimental

Gas atomized high purity (99.5%) AlCoCrFeNi HEA powder (Elemental Metals, average particle size 20 µm) is mixed 1:1 by volume with a transparent (crucial to enable higher energy absorption in the presence of powder particles) ultraviolet (UV) sensitive triethylene glycol dimethacrylate (TEGDMA) based resin. This slurry serves as the feedstock for a stereolithographic 3D printer equipped with a monochromatic LCD mask that cures the resin at a wavelength of 405 nm. The monochromatic mask provides an enhanced energy input to cure the slurry with the powder particles, augmenting the transmission of UV light navigating around the alloy powder. To improve adhesion to the build plate, we cure the resin without powder particles for the first few (~ 10) layers followed by curing the slurry, layer by layer, to form a sturdy green composite pellet of 10 mm in diameter. These pellets are baked at 550 °C for 4 h to extract the solvent (green part) in a flowing argon atmosphere at 40 psi (2.7 atm.) and create a green part free from resin. Further, the green part is sintered at an optimum temperature of 1200 °C for 24, 48, and 96 h to promote densification assisted by the neck formation and growth. A pictographic representation of the synthesis is included in Fig. 1. Additional procedural details on experimental design are provided as Supplementary Information.

These sintered pellets are mounted and polished (180 to 1200 grit SiC and colloidal silica) to eliminate surface oxides and prepare the samples for metallographic characterization. XRD (Pananalytical; Cu-Kα target

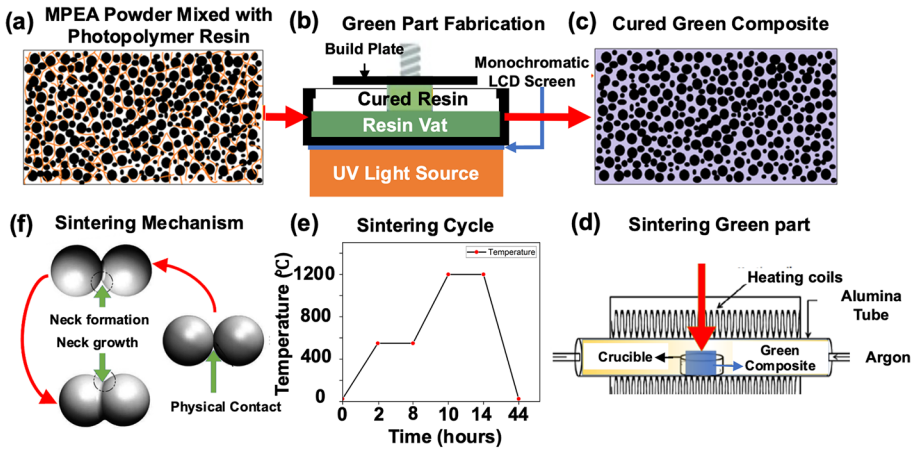

Fig. 1 Schematic of thermal solvent extraction using SLA-based AM: **a** AlCoCrFeNi powder particles are mixed in a transparent photopolymer resin with a resin to powder ratio of 1:1 by volume. **b** The mixed slurry is cured layer-by-layer using SLA-based AM technique to obtain a cured green composite (**c**). **d** The green composite is baked for 4 h at 550 °C to evaporate the resin retaining the green part ready for sintering. **e** The sintering cycle shows the temperatures and times the green part is subjected to during baking and sintering. Optimum conditions for sintering are found to be at 1200 °C for 24 h followed by furnace cooling. **f** A pictorial representation of the sintering mechanism to demonstrate the initiation of the physical contact, followed by the neck formation and growth densifying the component (Color figure online)

at $\lambda = 1.54$ nm), scanning electron microscopy (SEM) (Hitachi 4300SE), and energy dispersive X-Ray Spectroscopy (EDS, Octane elite) are performed to identify the phase, microstructure, and the composition of the synthesized HEA. The density of the samples is measured using an in-house setup with a high accuracy of 6 decimal places. Vickers microhardness (Leco LM 248) measurements are performed at 10 gf with a dwell time of 10 s. The particle size of gas atomized powder and sintered samples is analyzed using ImageJ. Also, the fabricated samples are compared against arc-melted AlCoCrFeNi HEAs.

Results and Discussion

The observations from the SEM and EDS characterizations of AlCoCrFeNi HEA powder particles with average particle size of ~ 20 µm, are presented in Fig. 2a–c. The powder particles are near-spherical with a few satellite particles on the surface. Cross-sectional analysis from the EDS reveals dense particles with a homogeneous distribution of the constituent elements with a near equiatomic composition (Table 1). XRD on the as-received powder and samples sintered over various times *i.e.,* 24, 48, 96 h, are reproduced in Fig. 2d. The as-received powder exhibits a BCC phase, but after prolonged sintering, peaks corresponding to the oxides of Al and Cr are recorded. The broadening in XRD peaks is attributed to the interplay of finite crystal size of powder particles, the internal stresses from non-uniform solidification, and the finer-scale grain/defect morphologies [39–41]. The peak shift suggests stabilization of the alloys sintered for 24, 48, and 96 h through a transformation of the BCC to FCC phases. We also note from the XRD that the proportions of FCC/oxides in the samples increase with increased sintering times. To deeply probe of this phase conversion, we further scrutinize the SEM and EDS results of the sintered samples.

Table 1 Elemental composition of AlCoCrFeNi powder validating near equiatomic composition

Element	Fe	Co	Ni	Al	Cr
At.%	20.37	18.88	18.31	20.92	21.52

Note that although we perform SEM characterization on all three samples, sintered respectively for 24, 48, and 96 h, we primarily interrogate the former that assumes an optimum density (~ 4.3 g/cm^3, ~ 62% of fully dense component) with minimal oxidation and notable hardness (~ 400 HV). The SEM images (Fig. 3a–d) reveal a dense part with well-connected powder particles, and the occurrence of a naturally aspired porosity resulting from resin evaporation. Figure 3c, d show the SEM micrographs of the sintered samples at different magnifications highlighting the neck formation and the welding of smaller particles between large particles. The sintering process, executed in a vacuum environment, recreates an impressive quality for the neck formation via this pressure-less sintering. The surface energy of particles is inversely correlated to their radii. Figure 2c indicates an abundance of powder particles with diameters < 10 µm. These small particles support sintering via welding between

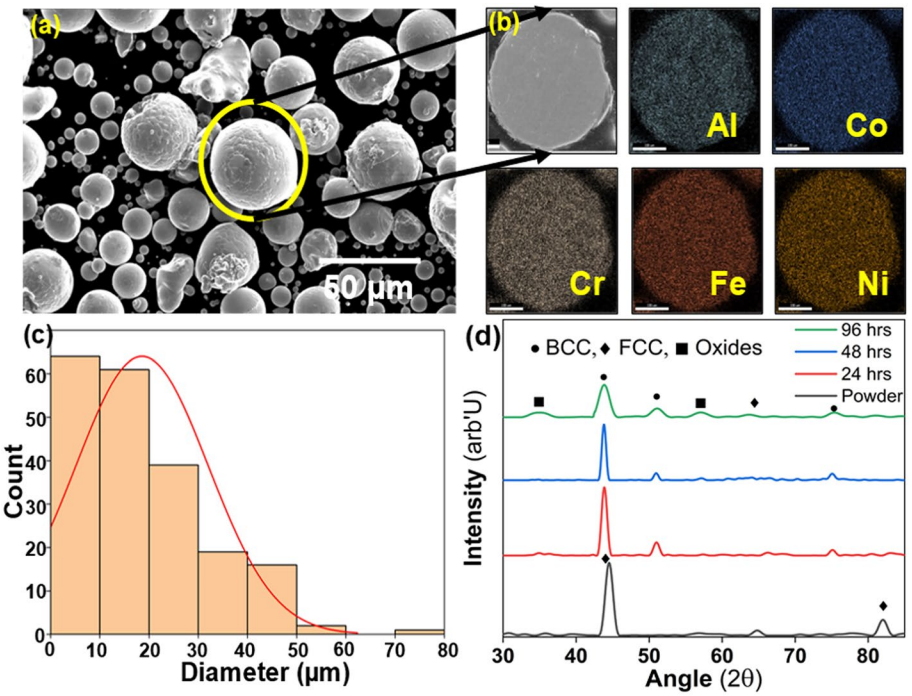

Fig. 2 Microscopic characterization of the powder particles. **a** SEM images of the powder shows that the particles are near-spherical in shape with a few satellite particles on their surfaces. **b** EDS analysis on the cross-section reveals dense powder particles with a homogenous composition and distribution of candidate elements. **c** The particle size distribution of powder particles assumes an average particle size of ~ 20 µm with a significant number of particles < 10 µm in diameter. **d** XRD of AlCoCrFeNi powder and sintered samples for 24, 48 and 96 h

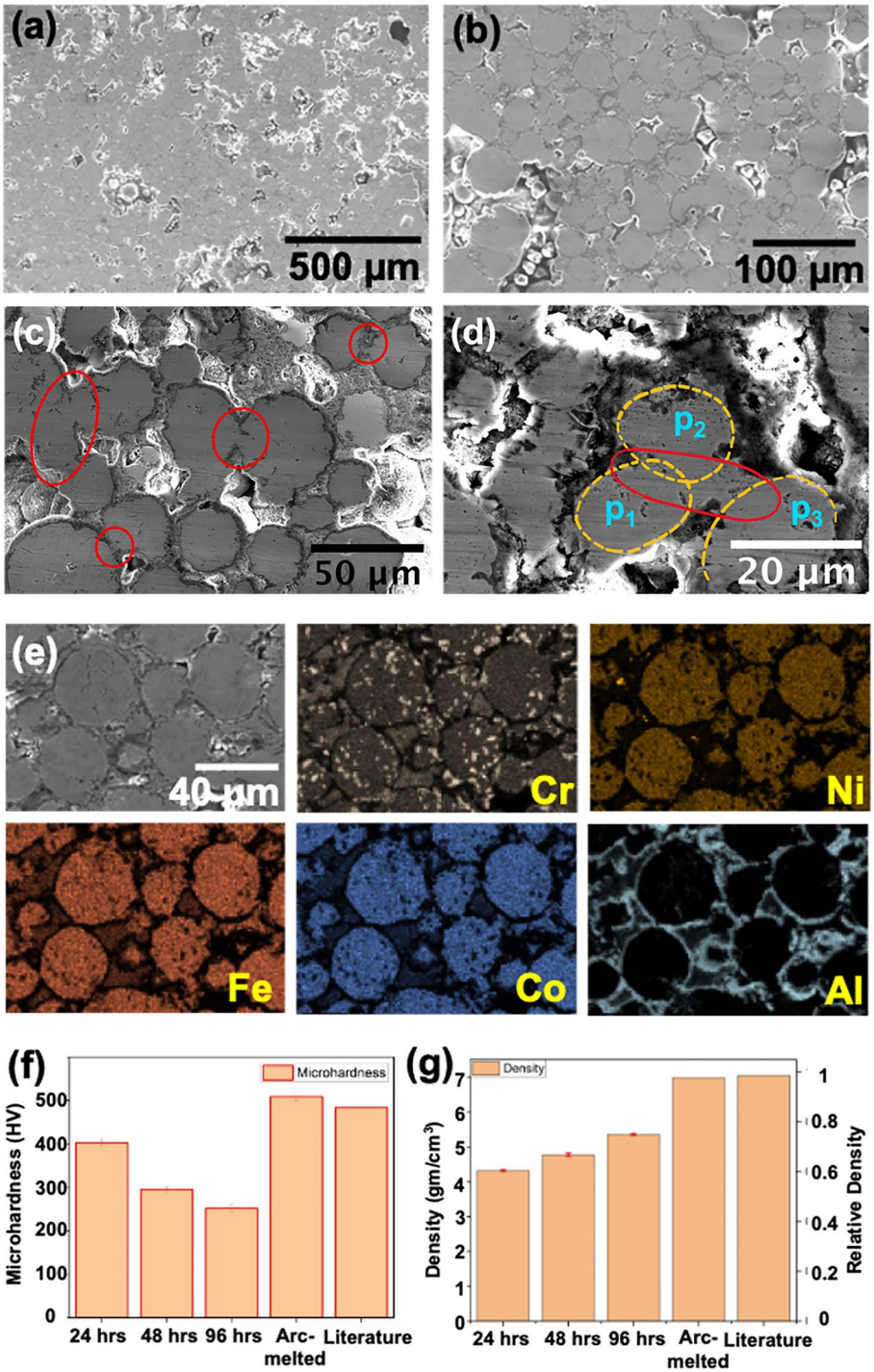

Fig. 3 Microscopic characterization of the sintered alloy. **a**, **b** SEM investigation of sintered part at 24 h indicates well-connected powder particles with a notable porosity (see Fig. S2 in Supplementary Information), **c**, **d** Magnified images of (**b**) reveal the formation and growth of the neck (circled in red). The smaller particles are consumed by larger counterparts (particles p_1 and p_2 are joined to particle p_3 via various coalesced small particles) through a diffusion mechanism at elevated temperatures. **e** EDS map of the sintered part uncovers a concentration of Al and Cr on the surface of the alloy while Cr, Co, Fe, and Ni are distributed within the material. **f** Microhardness measurements of the samples sintered at various times produce the highest hardness ~ 400 HV at 24 h of sintering time, with a density ~ 4.3 g/cm^3. The hardness reduces with increasing sintering time, while increasing the density simultaneously. **g** Density and relative density of sintered parts as compared with arc melted value (Color figure online)

larger particles as described by the red circles in Fig. 3c, d. From the SEM micrographs on porous Fe and Mg-Fe based scaffolds reported by Putra et al., it can be seen that smaller particles weld on/in-between larger particles that augments the sintering process [32, 33]. The surface energy of small particles is higher relative to larger particles, and this additional energy reduces the activation energy for the onset of diffusion and leads to the formation of a neck between particles. Once the larger particles are connected via a small particle, diffusion initiates and these smaller particles are consumed in the process which leads to the densification of the alloy. A similar trend in grain size growth is reported for CoCrFeNiMn HEA [31].

Similar findings for neck formation with binder jetting followed by sintering of CoCrFeMnNi HEA are available in the literature [42]. We juxtapose the similarity in necking

and the initial bonding between the results presented here and Xu et al.'s report [20]. As the temperature increases, the powder particles adhere to each other initiating a neck. Using molecular dynamics simulations, we have elucidated, elsewhere, that when particles come in contact, the necking initiates at a lower temperature and subsequent heating promotes the neck growth instigated from this contact, thereby densifying the material [43]. Additionally, it was discovered that for AlCoCrFeNi HEA there is a noticeable increase in neck diameter between 827 and 1077 °C [26]. However, in this study, we conducted sintering at temperatures of 1200 °C, 1225 °C, 1250 °C, 1275 °C, and 1300 °C. We determined that 1200 °C is the optimal sintering temperature, which closely aligns with molecular dynamics (MD) simulations ~ 1077 °C. The neck formation process initiates at the point of initial contact during resin removal at 550 °C. Subsequent diffusion is facilitated by the high surface energy (2.3 J/m^2 at 1077 °C, as predicted by first-principles calculations [26]), and it is primarily driven by the elevated temperature. In addition, the process induces a naturally aspired porosity based on the powder packing and the resin-to-powder ratio (Fig. 3a), resulting in a reduced density and weight. We note surface oxidation of Al and Cr present in the sample through the EDS maps (Fig. 3e). We use high purity research-grade Ar gas to extract the green part from the resin; nonetheless, trace amounts of oxygen are present in the gas, causing oxygen to be trapped on the surfaces of the powder particles that subsequently promote the formation of Al based and traces of Cr-based oxides at higher temperatures (see Fig. S3 in Supplementary Information). However, these passivating surface oxides render the alloy resistant to further oxidation due to the high surface area resulting from the low density. In principle, similar oxidation mechanism can be leveraged with tailored compositions, where powder particles coated with oxidizing agents can enable passivating surface oxides, while the bulk alloy is able to reproduce structural properties and endure harsh environments at elevated temperatures.

The above-discussed BCC to FCC phase transformation by surface oxide formation contribute to the reduction in the alloy hardness. Figure 3f, g displays the Vickers microhardness and average density of the sintered pellets, respectively. The porosity is estimated using the SEM micrographs of the sintered pellets and represented as percentage porosity in Fig. S1 of the Supplementary Information. Given that porosity reduces with increased sintering time, our results are in close agreement with findings in the literature for a different processing modality [34]. We corroborate from Fig. 3a–e that the powder particles undergo a robust sintering at a 1200 °C for 24 h, and any further sintering increases the possibility of gradual oxidation that reduces the hardness of the samples (Fig. 3f). The oxidation causes depletion of Al in the alloy powder, which otherwise would have stabilized the BCC phase [44]. Various fractions for Al have been extensively mixed with Co–Cr–Fe–Ni based MPEAs to improve the hardness and trigger the transformation to a dominant BCC phase in HEAs [45–48] phase in HEAs [45–48]. Thus, we establish 24 h to be the optimal time for the sintering and the manufacture of lightweight and high-hardness porous AlCoCrFeNi HEAs.

Conclusion

In summary, we reiterate that to realize the promise that MPEAs have demonstrated with the exceptional mechanical and catalytic properties of some of the compositions, pathways to manufacture them with reduced density is critical. While architected, hierarchical, and cellular structures can address some of the associated challenges by producing lightweight alloys, the costs associated with scalable production of these components is high due to specialized skills and the difficulty in procuring suitable equipment. We present a cost-efficient thermal-solvent extraction based AM technique that produces low-density MPEAs with porous structures. A pre-alloyed powder of AlCoCrFeNi HEA is mixed in a transparent photopolymer resin that is used in the SLA process to synthesize a cylindrical green specimen. The latter is baked at 550 °C to extract the green part free from the resin, and further heated in a vacuum environment at 1200 °C to promote sintering by the formation and growth of the neck. The part sintered for 24 h exhibits BCC and FCC phases together with surface oxides of Al (prominent) and Cr (traces), and assumes a hardness ~ 400 HV and density ~ 4.3 g/cm^3. SEM characterization reveals a well-connected sintered part with passivating surface oxides on the powder particles, which is advantageous to the alloy under high temperature and oxidizing environments. Increasing the sintering time beyond 24 h reduces the hardness while promoting oxidation, which is detrimental to the alloy part. A wide range in the particle size distribution contributes to the manufacturing process by enhancing the sintering mechanism, wherein the smaller particles serve as fillers to weld larger particles. Further research is essential to understand the effect of different particle size distributions on the properties of the sintered parts. A deeper understanding of thermal expansion and conductivities for these materials is needed to design parts with higher geometric precision. Investigating the corrosion behavior in the presence of biological fluids is imminent for assessing the suitability of these materials for use in bio implants. This customizable fabrication method for biomedical implants presents a cost-effective alternative compared to conventional AM techniques such as selective laser melting, laser powder bed fusion, wire arc and electron beam manufacturing. Its efficiency and adaptability make it a promising approach for meeting physiological requirements in implant

applications. This AM technique holds advantages over the other approaches in terms of process simplicity, throughput, and potential scalability.

Supplementary Information The online version contains supplementary material available at https://doi.org/10.1007/s44210-024-00029-z.

Acknowledgements The research was supported by the National Science Foundation (NSF) through the award CMMI-1944040.

Author Contributions PS: Methodology, Formal Analysis, Investigation, Validation, Writing—Original Draft, Writing—Review & Editing; CD: Methodology, Investigation; PS: Methodology, Validation, Writing—Review & Editing; GB: Formal Analysis, Investigation, Writing—Review & Editing, Supervision, Funding Acquisition.

Data Availability The authors will make available, upon request, the data used in the applications described in this work. It is understood that the data provided will not be for commercial use.

Declarations

Competing interests The authors declare no competing financial or non-financial interests.

References

1. B. Cantor, I.T.H. Chang, P. Knight, A.J.B. Vincent, Microstructural development in equiatomic multicomponent alloys. Mater. Sci. Eng. A **375–377**, 213–218 (2004). https://doi.org/10.1016/J.MSEA.2003.10.257
2. J.W. Yeh, S.K. Chen, S.J. Lin, J.Y. Gan, T.S. Chin, T.T. Shun, C.H. Tsau, S.Y. Chang, Nanostructured high-entropy alloys with multiple principal elements: novel alloy design concepts and outcomes. Adv. Eng. Mater. **6**, 299–303 (2004). https://doi.org/10.1002/ADEM.200300567
3. D.B. Miracle, O.N. Senkov, A critical review of high entropy alloys and related concepts. Acta Mater. **122**, 448–511 (2017). https://doi.org/10.1016/j.actamat.2016.08.081
4. P. Sharma, N. Naushin, S. Rohila, A. Tiwari, Magnesium containing high entropy alloys. in *Magnesium Alloys Structure and Properties* (IntechOpen, 2022). https://doi.org/10.5772/intechopen.98557
5. Y. Zhang, T.T. Zuo, Z. Tang, M.C. Gao, K.A. Dahmen, P.K. Liaw, Z.P. Lu, Microstructures and properties of high-entropy alloys. Prog. Mater. Sci. **61**, 1–93 (2014). https://doi.org/10.1016/j.pmatsci.2013.10.001
6. Z. Ye, C. Li, J. Gu, Phase stability in high-entropy alloys: the role of configurational entropy. JOM **74**, 4154–4161 (2022). https://doi.org/10.1007/s11837-022-05307-y
7. X. Yan, Y. Zhang, Functional properties and promising applications of high entropy alloys. Scr. Mater. **187**, 188–193 (2020). https://doi.org/10.1016/J.SCRIPTAMAT.2020.06.017
8. O. El-Atwani, N. Li, M. Li, A. Devaraj, J.K.S. Baldwin, M.M. Schneider, D. Sobieraj, J.S. Wróbel, D. Nguyen-Manh, S.A. Maloy, E. Martinez, Outstanding radiation resistance of tungsten-based high-entropy alloys. Sci Adv. **5**, eaav2002 (2019). https://doi.org/10.1126/SCIADV.AAV2002/SUPPL_FILE/AAV2002_SM.PDF
9. D. Zhang, H. Zhao, X. Wu, Y. Deng, Z. Wang, Y. Han, H. Li, Y. Shi, X. Chen, S. Li, J. Lai, B. Huang, L. Wang, D. Zhang, H. Zhao, X. Wu, Y. Deng, Z. Wang, Y. Han, H. Li, Y. Shi, J. Lai, L. Wang, X. Chen, S. Li, B. Huang, Multi-site electrocatalysts boost pH-universal nitrogen reduction by high-entropy alloys. Adv. Funct. Mater. **31**, 2006939 (2021). https://doi.org/10.1002/ADFM.202006939
10. X. Jin, J. Bi, L. Zhang, Y. Zhou, X. Du, Y. Liang, B. Li, A new CrFeNi2Al eutectic high entropy alloy system with excellent mechanical properties. J. Alloys Compd. **770**, 655–661 (2019). https://doi.org/10.1016/J.JALLCOM.2018.08.176
11. Y. Zhang, M. Liu, J. Sun, G. Li, R. Zheng, W. Xiao, C. Ma, Excellent thermal stability and mechanical properties of bulk nanostructured FeCoNiCu high entropy alloy. Mater. Sci. Eng. A **835**, 142670 (2022). https://doi.org/10.1016/J.MSEA.2022.142670
12. K.V. Yusenko, S. Riva, P.A. Carvalho, M.V. Yusenko, S. Arnaboldi, A.S. Sukhikh, M. Hanfland, S.A. Gromilov, First hexagonal close packed high-entropy alloy with outstanding stability under extreme conditions and electrocatalytic activity for methanol oxidation. Scr. Mater. **138**, 22–27 (2017). https://doi.org/10.1016/J.SCRIPTAMAT.2017.05.022
13. S. Dixit, S. Rodriguez, M.R. Jones, P. Buzby, R. Dixit, N. Argibay, F.W. DelRio, H.H. Lim, D. Fleming, Refractory high-entropy alloy coatings for high-temperature aerospace and energy applications. J. Therm. Spray Technol. **31**, 1021–1031 (2022). https://doi.org/10.1007/S11666-022-01324-0/FIGURES/8
14. K.R. Lim, K.S. Lee, J.S. Lee, J.Y. Kim, H.J. Chang, Y.S. Na, Dual-phase high-entropy alloys for high-temperature structural applications. J. Alloys Compd. **728**, 1235–1238 (2017). https://doi.org/10.1016/J.JALLCOM.2017.09.089
15. A.E. Afolabi, A.P.I. Popoola, O.M. Popoola, High entropy alloys: advance material for landing gear aerospace applications, in *Handbook of Nanomaterials and Nanocomposites for Energy and Environmental Applications* (Springer, Cham, 2020), pp. 1–27. https://doi.org/10.1007/978-3-030-11155-7_179-1
16. C.L.P. Pavithra, S.R. Dey, Advances on multi-dimensional high-entropy alloy nanoarchitectures: unconventional strategies and prospects. Nano Select. **4**, 48–78 (2023). https://doi.org/10.1002/nano.202200081
17. I. Gibson, D. Rosen, B. Stucker, M. Khorasani, Development of additive manufacturing technology. in *Additive Manufacturing Technologies* (Springer, Cham, 2021), pp. 23–51. https://doi.org/10.1007/978-3-030-56127-7_2
18. W.E. Frazier, Metal additive manufacturing: a review. J. Mater. Eng. Perform. **23**, 1917–1928 (2014). https://doi.org/10.1007/s11665-014-0958-z
19. W. Tao, M.C. Leu, Design of lattice structure for additive manufacturing. in *2016 International Symposium on Flexible Automation (ISFA), IEEE*, 2016, pp. 325–332. https://doi.org/10.1109/ISFA.2016.7790182
20. A. Kumar, L. Collini, A. Daurel, J.-Y. Jeng, Design and additive manufacturing of closed cells from supportless lattice structure. Addit. Manuf. **33**, 101168 (2020). https://doi.org/10.1016/j.addma.2020.101168
21. Z.U. Arif, M.Y. Khalid, E. ur Rehman, Laser-aided additive manufacturing of high entropy alloys: processes, properties, and emerging applications. J. Manuf. Process. **78**, 131–171 (2022). https://doi.org/10.1016/j.jmapro.2022.04.014
22. C. Kenel, N.P.M. Casati, D.C. Dunand, 3D ink-extrusion additive manufacturing of CoCrFeNi high-entropy alloy micro-lattices. Nat. Commun. **10**, 904 (2019). https://doi.org/10.1038/s41467-019-08763-4
23. S.Y. Ahn, F. Haftlang, E.S. Kim, J.S. Lee, S.G. Jeong, J.B. Seol, H. Choi, H.S. Kim, Cellular structure engineering of additive manufactured CoCrFeMnNi high-entropy composite: the role of hard ceramic reinforcements in elemental segregation of constitutive elements. Addit. Manuf. Lett. **7**, 100172 (2023). https://doi.org/10.1016/j.addlet.2023.100172

24. W. Li, Y. Huang, Z. Xie, H. Chen, W. Li, B. Liu, B. Wang, Mechanical property and cellular structure of an additive manufactured FeCoNiCrMo0.2 high-entropy alloy at high-velocity deformation. J. Mater. Sci. Technol. **139**, 156–166 (2023). https://doi.org/10.1016/j.jmst.2022.08.013
25. S. Peng, S. Mooraj, R. Feng, L. Liu, J. Ren, Y. Liu, F. Kong, Z. Xiao, C. Zhu, P.K. Liaw, W. Chen, Additive manufacturing of three-dimensional (3D)-architected CoCrFeNiMn high- entropy alloy with great energy absorption. Scr. Mater. **190**, 46–51 (2021). https://doi.org/10.1016/j.scriptamat.2020.08.028
26. C. Han, Q. Fang, Y. Shi, S. Beng Tor, C. Kai Chua, K. Zhou, C. Han, S.B. Tor, K. Zhou, Q. Fang, Y. Shi, C.K. Chua, Recent advances on high-entropy alloys for 3D printing. Adv. Mater. **32**, 1903855 (2020). https://doi.org/10.1002/ADMA.201903855
27. S. Chen, Y. Tong, P.K. Liaw, Additive manufacturing of high-entropy alloys: a review. Entropy **20**, 937 (2018). https://doi.org/10.3390/E20120937
28. A. Ostovari Moghaddam, N.A. Shaburova, M.N. Samodurova, A. Abdollahzadeh, E.A. Trofimov, Additive manufacturing of high entropy alloys: a practical review. J. Mater. Sci. Technol. **77**, 131–162 (2021). https://doi.org/10.1016/J.JMST.2020.11.029
29. S. Guan, J. Ren, S. Mooraj, Y. Liu, S. Feng, S. Zhang, J. Liu, X. Fan, P.K. Liaw, W. Chen, Additive manufacturing of high-entropy alloys: microstructural metastability and mechanical behavior. J. Phase Equilibria Diffus. **42**, 748–771 (2021). https://doi.org/10.1007/s11669-021-00913-w
30. C. Kenel, N.P.M. Casati, D.C. Dunand, 3D ink-extrusion additive manufacturing of CoCrFeNi high-entropy alloy micro-lattices. Nat. Commun. **10**, 1–8 (2019). https://doi.org/10.1038/s41467-019-08763-4
31. Y. Zhang, T. Bian, X. Shen, Z. Wang, S. Ye, S. Feng, K. Yu, C. Ding, P. Yu, Sintering mechanism and microstructure evolution of a CoCrFeNiMn high entropy alloy fabricated by metal injection molding. J. Alloys Compd. **868**, 158711 (2021). https://doi.org/10.1016/J.JALLCOM.2021.158711
32. N.E. Putra, M.A. Leeflang, M. Minneboo, P. Taheri, L.E. Fratila-Apachitei, J.M.C. Mol, J. Zhou, A.A. Zadpoor, Extrusion-based 3D printed biodegradable porous iron. Acta Biomater. **121**, 741–756 (2021). https://doi.org/10.1016/J.ACTBIO.2020.11.022
33. N.E. Putra, M.A. Leeflang, P. Taheri, L.E. Fratila-Apachitei, J.M.C. Mol, J. Zhou, A.A. Zadpoor, Extrusion-based 3D printing of ex situ-alloyed highly biodegradable MRI-friendly porous iron-manganese scaffolds. Acta Biomater. **134**, 774–790 (2021). https://doi.org/10.1016/J.ACTBIO.2021.07.042
34. G.K. Meenashisundaram, Z. Xu, M.L.S. Nai, S. Lu, J.S. Ten, J. Wei, Binder jetting additive manufacturing of high porosity 316L stainless steel metal foams. Materials **13**, 3744 (2020). https://doi.org/10.3390/MA13173744
35. P. Mondal, A. Das, A. Wazeer, A. Karmakar, Biomedical porous scaffold fabrication using additive manufacturing technique: porosity, surface roughness and process parameters optimization. Int. J. Lightweight Mater. Manuf. **5**, 384–396 (2022). https://doi.org/10.1016/j.ijlmm.2022.04.005
36. R. Otto, C. Kiener, Y. Küsters, K. Sørby, Additive manufacturing of open porous functional structures: roadmap from manufacturing to the application. Procedia CIRP. **112**, 334–339 (2022). https://doi.org/10.1016/j.procir.2022.09.102
37. D. Ren, X. Ba, Z. Zhang, Z. Zhang, K. Zhao, L. Liu, Wire arc additive manufacturing of porous metal using welding pore defects. Mater. Des. **233**, 112213 (2023). https://doi.org/10.1016/j.matdes.2023.112213
38. Y.C. Wu, C.N. Kuo, M.Y. Shie, Y.L. Su, L.J. Wei, S.Y. Chen, J.C. Huang, Structural design and mechanical response of gradient porous Ti-6Al-4V fabricated by electron beam additive manufacturing. Mater. Des. **158**, 256–265 (2018). https://doi.org/10.1016/j.matdes.2018.08.027
39. K. Kusada, H. Kobayashi, R. Ikeda, Y. Kubota, M. Takata, S. Toh, T. Yamamoto, S. Matsumura, N. Sumi, K. Sato, K. Nagaoka, H. Kitagawa, Solid solution alloy nanoparticles of immiscible Pd and Ru elements neighboring on Rh: changeover of the thermodynamic behavior for hydrogen storage and enhanced CO-oxidizing ability. J. Am. Chem. Soc. **136**, 1864–1871 (2014). https://doi.org/10.1021/ja409464g
40. W. Ji, W. Qi, S. Tang, H. Peng, S. Li, Hydrothermal synthesis of ultrasmall Pt nanoparticles as highly active electrocatalysts for methanol oxidation. Nanomaterials **5**, 2203–2211 (2015). https://doi.org/10.3390/nano5042203
41. D. Wu, K. Kusada, Y. Nanba, M. Koyama, T. Yamamoto, T. Toriyama, S. Matsumura, O. Seo, I. Gueye, J. Kim, L.S. RosanthaKumara, O. Sakata, S. Kawaguchi, Y. Kubota, H. Kitagawa, Noble-metal high-entropy-alloy nanoparticles: atomic-level insight into the electronic structure. J. Am. Chem. Soc. **144**, 3365–3369 (2022). https://doi.org/10.1021/jacs.1c13616
42. Z. Xu, Z. Zhu, P. Wang, G.K. Meenashisundaram, S.M.L. Nai, J. Wei, Fabrication of porous CoCrFeMnNi high entropy alloy using binder jetting additive manufacturing. Addit. Manuf. **35**, 101441 (2020). https://doi.org/10.1016/J.ADDMA.2020.101441
43. P. Sreeramagiri, P. Sharma, C. Das, G. Balasubramanian, Examining solid-state sintering of AlCoCrFeNi multi-principal element alloy by molecular simulations. Comput. Mater. Sci. **216**, 111875 (2023). https://doi.org/10.1016/j.commatsci.2022.111875
44. T.M. Butler, M.L. Weaver, Oxidation behavior of arc melted AlCoCrFeNi multi-component high-entropy alloys. J. Alloys Compd. **674**, 229–244 (2016). https://doi.org/10.1016/J.JALLCOM.2016.02.257
45. W.R. Wang, W.L. Wang, S.C. Wang, Y.C. Tsai, C.H. Lai, J.W. Yeh, Effects of Al addition on the microstructure and mechanical property of AlxCoCrFeNi high-entropy alloys. Intermetallics **26**, 44–51 (2012). https://doi.org/10.1016/J.INTERMET.2012.03.005
46. Y.F. Kao, T.J. Chen, S.K. Chen, J.W. Yeh, Microstructure and mechanical property of as-cast, -homogenized, and -deformed AlxCoCrFeNi ($0 \leq x \leq 2$) high-entropy alloys. J. Alloys Compd. **488**, 57–64 (2009). https://doi.org/10.1016/J.JALLCOM.2009.08.090
47. C. Li, J.C. Li, M. Zhao, Q. Jiang, Effect of aluminum contents on microstructure and properties of AlxCoCrFeNi alloys. J. Alloys Compd. **504**, S515–S518 (2010). https://doi.org/10.1016/J.JALLCOM.2010.03.111
48. T. Yang, S. Xia, S. Liu, C. Wang, S. Liu, Y. Zhang, J. Xue, S. Yan, Y. Wang, Effects of AL addition on microstructure and mechanical properties of AlxCoCrFeNi High-entropy alloy. Mater. Sci. Eng. A **648**, 15–22 (2015). https://doi.org/10.1016/J.MSEA.2015.09.034